ISSN 1392–124X (print), ISSN 2335–884X (online) INFORMATION TECHNOLOGY AND CONTROL, 2016, T. 45, Nr. 3

Highly Convergent Finite Elements with Diagonal Mass Matrix for Short Wave Pulse Propagation Simulation

Andrius Kriščiūnas, Rimantas Barauskas

Department of Applied Informatics, Kaunas University of Technology
Studentų str. 50, LT-51368 Kaunas, Lithuania
e-mail: andrius.krisciunas@ktu.lt

crossref http://dx.doi.org/10.5755/j01.itc.45.3.13557

Abstract. The modal-synthesis based approach is employed for obtaining the higher-order dynamic 1D finite elements with enhanced convergence properties. The obtained dynamic models are used for modelling short transient waves and wave pulses propagating in elastic or acoustic environments by using rough space steps. Only few nodal points per pulse length are enough for obtaining reasonable simulation results. The main advantage of the created elements compared with earlier similar approach lies in usage of the diagonal mass matrix of the element. The elements are compatible with conventional finite elements, may be used in branchy non-homogenous structures, as well as enable to implement non-reflecting boundary conditions. The saving the computational resources is estimated.

Keywords: wave propagation; finite elements; modal synthesis; phase velocity error.

1. Introduction

Finite element (FE) simulations of wave propagation (WP) in elastic or acoustic media are of significant importance in engineering applications, such as ultrasonic measurement procedures [6,14,17] pressure pulses propagation in large structures or pipe networks, etc. Computational WP models are based on the general structural dynamics equations and may be explored by applying the structural vibration analysis techniques. However, the very nature of real WP problems may raise specific challenges despite the illusory simplicity of the models, which in many cases can be based on small strain and linear material behavior assumptions. Here we concentrate on the multi-scale problem, where the simulated wavelengths are many times smaller than the dimensions of the body, in which the WP is investigated. Simulations of practical value require the models of huge dimensionality. As direct multi-scale approaches cannot be applied in short WP problems, only the roughness of the mesh determines the dimensionality of the computational model. It is known that the conventional first-order finite elements require ~20-30 space steps per shortest simulated wavelength in order to obtain adequate simulation results, and smallest 2D problems of any practical value require to use $10^6 - 10^7$ elements. Rougher meshes tend to increase the simulation errors, which exhibit themselves as severe deterioration of the shapes of propagating wave pulses as the time of simulation increases. This happens due to the errors of representation of wave propagation velocities of different harmonic components of the propagating pulse. The magnitude of the error depends on the number of elements per wavelength. The relationship of the wave velocity against the wave frequency or against the wavelength is referred to as the dispersion curve, therefore the errors under consideration are often referred to as numerical dispersion errors (NDE) or phase velocity errors.

The complete elimination of ND errors is possible by applying semi-analytical FE approach to WP problems [3]. However, this works only for WP along uniform cross-sectional shape waveguides and is not applicable for general 2D or 3D problems, as well as in the case of varying along the waveguide cross-section in 1D. The approaches based on structural dynamic models are based on the higher order FE, which could ensure the accuracy of simulation results within acceptable limits. In [18], it was demonstrated that the positions of the higher-order finite element nodes are of great importance, where equidistant, Lobatto and Chebyshev node distributions were investigated. In [7] the general template was proposed for retrieving characteristic matrices of n-node bar elements, based on their reduced diagonal representations. In [9] B-spline modification of FEM has been investigated by using complex wavenumber Fourier analysis, where NDE were minimized. In [12] the technique for the elimination of transient wave reflections from the

boundaries of small sub-models was used in order to assemble a large structure in a computationally efficient manner. In [8] the advantages of FE and spectral methods were combined in the case of 1D linear problem. In [5] the research was extended for 2D problems. In [4] B-spline wavelet on interval finite element has been applied for the analysis of elastic wave propagation in 1D structure. In [16] NDE were minimized by sub-gridding finite difference scheme for solving the Helmholtz equation with perfectly matched layer in the two dimensional domain. In [11] NDE analysis for FE models in time domain was performed. The optimum time step has been found, which minimizes the phase error introduced by the nonlinear dispersion relation.

The approach presented in this work is based on synthesized finite elements (SE) as in our earlier research [1]. SE were synthesized on the base of appropriately modified modal frequencies (MF) and modal shapes (MS) of the component substructures assembled of conventional linear finite elements (CFE). The way and extent of modification of MF and MS was established by solving the optimization problem, where the modal errors of the component substructure were minimized. It was demonstrated that the percentage of close to accurate structural modes was preserved as large structures were assembled of SE. In case the model assembled of SE contained about 80% of the modes the errors of which did not exceed 2%, the mesh containing only 6-10 elements per wavelength could be used, and the propagating wave pulse retained its original shape over large propagation distances. The approach originally demonstrated on 1D WP models was later extended to 2D [2]. The main drawback of the SE approach was that the mass matrices were non-diagonal and unable to fully exploit the advantages of explicit time integration schemes. An essential point of this work is the modified algorithm for obtaining SE, where only the stiffness matrix is synthesized while the mass matrix remains diagonal. SE exhibit similar convergence properties in branched 1D structures, as well as can be combined with CFE in order to implement the non-reflecting boundary conditions.

2. Synthesis of the finite element

The finite element model of wave propagation in elastic bodies can be presented in the form of the general structural dynamic equation system

$$[\mathrm{M}]\{\ddot{\mathrm{U}}\} + [\mathrm{C}]\{\dot{\mathrm{U}}\} + [\mathrm{K}]\{\mathrm{U}\} = \{\mathrm{F(t)}\} \qquad (1)$$

where $[\mathrm{M}]$, $[\mathrm{C}]$ and $[\mathrm{K}]$ are mass, damping and stiffness matrices, $\{\mathrm{U}\}$ is the nodal displacement vector and $\{\mathrm{F(t)}\}$ is the excitation force vector.

In the case of small damping, the influence of the damping matrix on the eigenvalues and eigenvectors of the model is also small, therefore we assume $[\mathrm{C}] = [\mathbf{0}]$ while the element matrices are calculated. Further small damping can be presented in the proportional form $[\mathrm{C}] = a[\mathrm{M}] + \beta[\mathrm{K}]$, where a, β are coefficients.

Modal frequencies (MF) and modal shapes (MS) of the structure are obtained by solving the eigenvalue problem as

$$([\mathrm{K}] - \omega^2[\mathrm{M}])\{\mathrm{y}\} = \{0\} \qquad (2)$$

where ω – modal frequency, $\{\mathrm{y}\}$ – modal shape.

Real symmetric structural matrices $[\mathrm{M}]$ and $[\mathrm{K}]$ ensure the solutions of (2) as n structural modes $\omega_i, \{y_i\}, i = 1, \dots, n$. The fundamental properties of structural modes provide that matrices $[\mathrm{M}]$ and $[\mathrm{K}]$ can be expressed in terms of normalized MS and MF as

$$[\mathrm{M}] = ([\mathrm{Y}]^{\mathrm{T}})^{-1}[\mathrm{Y}]^{-1} \qquad (3.1)$$

$$[\mathrm{K}] = ([\mathrm{Y}]^{\mathrm{T}})^{-1}[\mathrm{diag}(\omega_1{}^2, \omega_2{}^2, \dots, \omega_{\mathrm{n}}{}^2)][\mathrm{Y}]^{-1} \qquad (3.2)$$

where $[\mathrm{Y}] = [\{y_1\}, \{y_2\}, \dots, \{y_n\},]$ is the matrix of MS.

This means that the matrices of an element or of the structure can be generated by directly referring to the known or desired values of MF and MS. In case we know the first exact MF and MS of the investigated domain, the NDE of the structural model created as (3) equals zero for all wave frequencies within the range of the employed MF. However, in most cases it is hardly possible to calculate the necessary number of modes of the whole domain, therefore such an approach is of poor practical value. The approach regains the practical value in case the matrices of the computational domain are assembled of the matrices of subdomains, which are synthesized by using the appropriate MF and MS. Such subdomains are referred to as synthesized finite elements (SE).

The outline of the synthesis procedure is presented in **Fig. 1**. The computational domain is divided into component substructures (CS) of simple geometry of $\widetilde{N}$ d.o.f. each. The external geometrical shape of the CS is the same as of the SE we are going to create. However, the number of d.o.f. of the SE must be much smaller, $N \ll \widetilde{N}$. The high mesh refinement of the CS is necessary for ensuring the high accuracy of its first n modes in case the CS is treated as a stand-alone structure. The matrices of SE are computed by means of relation (3), where the first n close-to-exact modes obtained from the highly refined CS model are used. As (3) is applied, the MS available in highly refined mesh of the CS are mapped upon much rougher mesh of the SE in a proper manner. It is worth to mention that, for simple geometries of CS, the necessary number of its exact modes sometimes can be obtained analytically.

The SE obtained in this way is referred to as the initial approximation element (IAE). By using IAEs, a model of any required geometry could be assembled. Unfortunately, the errors of models assembled of close-to-exact IAEs are significant. Therefore we enter the optimization loop, where the MS used for the synthesis of SE are treated as optimization parameters. The MS are slightly modified during each

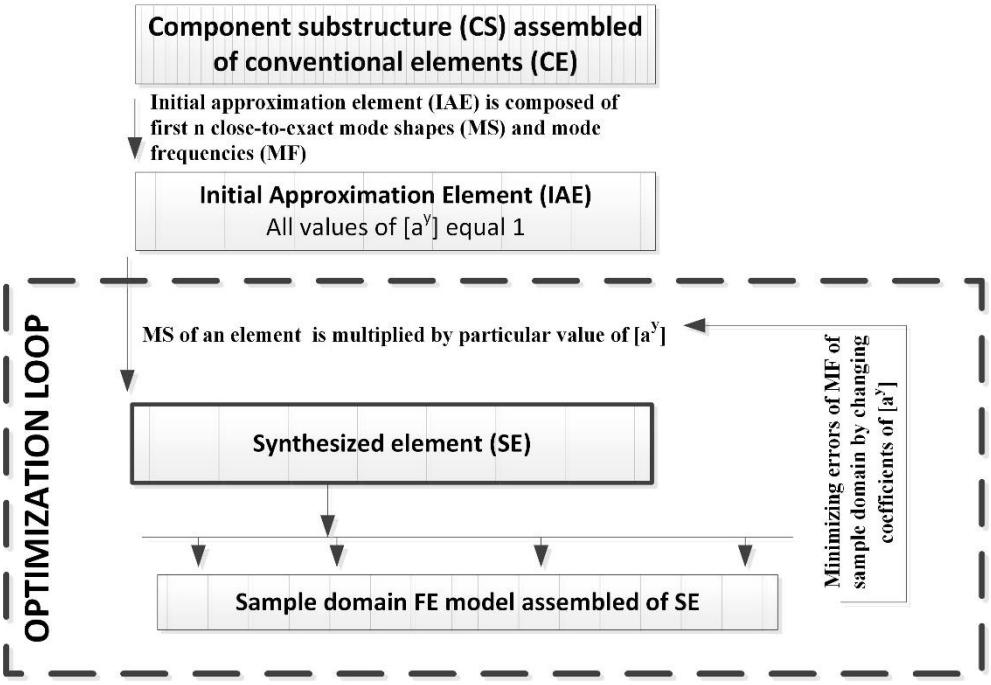

Figure 1. Outline of the SE generation procedure

optimization loop in order to ensure that a certain reference structure, or sample domain (SD) assembled of a certain number of SEs provides as many as possible close-to-exact modes. At the first sight, we could suspect that the result is dependent on the selected size and shape of the SD, which we may select freely. Fortunately, we found that the dependence of the result on the number of SEs used in the SD is not significant. E.g. in 1D case we may intend to synthesize a 10-noded SE. For obtaining the proper modification of the modal shapes, the optimization problem is solved, where 91-noded SD assembled of 10 such SEs is used as a reference structure. We must know the close-to-exact modal shapes of the SD, however this can be calculated once by using a very dense mesh or sometimes can be obtained analytically. Anyway, the number of d.o.f. N of the SD may be selected much smaller than the number of d.o.f. of the real computational domain of practical value.

The optimization loop in **Fig. 1** is used for the minimization of the target function, which presents the cumulative error of modal frequencies of the SD as

$$\min_{[a^y]} \Psi = \sum_{i=1}^{\tilde{N}} \left(\frac{\hat{\omega}_i - \omega_{i0}}{\omega_{i0}}\right)^2 \quad (4)$$

where ω_i are the MFs of the SD assembled of SE, ω_{i0} are close-to-exact MFs of the SD, and $[a^y]$ is the matrix of MS correction coefficients treated as optimization variables. The summation of errors is performed over $\tilde{N} \leq N$ modal frequencies of the SD.

The correction of MS is performed as

$$[\{\tilde{y}_{11}, \dots, \tilde{y}_{1n}\}, \dots, \{\tilde{y}_{n1}, \dots, \tilde{y}_{nn}\}] = [\{y_{11} * a_{11}^y, \dots, y_{1n} * a_{1n}^y\}, \dots, \{y_{n1} * a_{n1}^y, \dots, y_{nn} * a_{nn}^y\}] \quad (5)$$

where each j-th term of i-th MS is multiplied by the corresponding value taken from matrix $[a^y]$. Corrections of all MSs are performed with exception of the rigid-body modal shapes, which correspond to zero modal frequencies.

Minimization of the target function (4) is performed by using the gradient descent method. The gradient $\frac{\delta\Psi}{\delta[a^y]}$ is expressed as

$$\delta\Psi = \sum_{i=1}^{N} \frac{\hat{\omega}_i - \hat{\omega}_{i0}}{\hat{\omega}_{i0}\hat{\omega}_i} \delta\hat{\omega}_i^2 \quad (6)$$

$$\delta\hat{\omega}_i^2 = \{\tilde{y}_i\}^T \left(\frac{\partial[\hat{K}]}{\partial\alpha} - \hat{\omega}_i^2 \frac{\partial[\hat{M}]}{\partial\alpha}\right)\{\tilde{y}_i\}. \quad (7)$$

As we do not change mass matrix in order to preserve its diagonal form, $\frac{\partial[\hat{M}]}{\partial\alpha} = 0$ is assumed. From equations (6) and (7), the gradient $\frac{\delta\Psi}{\delta a_{ij}^y}$ is expressed as

$$\frac{\delta\Psi}{\delta a_{ij}^y} = \sum_{i=1}^{N} \sum_{j=1}^{N} \frac{\hat{\omega}_i - \hat{\omega}_{i0}}{\hat{\omega}_{i0}\hat{\omega}_i} \{\tilde{y}_i\}^T \left(\frac{\partial[\hat{K}]}{\partial a_{ij}^y}\right)\{\tilde{y}_i\} \quad (8)$$

where $[\hat{K}]$ is assembled in each optimization step of the SE matrices obtained at previous optimization step.

The derivative $\frac{\partial[\hat{K}]}{\partial a_{ij}^y}$ is expressed as

$$\frac{\partial[\hat{K}]}{\partial a_{ij}^y} = -\left(\{a^y\}^T[\tilde{Y}]^T\right)^{-1} \left([0, \dots, 0, y_{ij}, 0, \dots, 0][\hat{K}][\tilde{Y}]\{a^y\} + \{a^y\}^T[\tilde{Y}]^T[\hat{K}][0, \dots, 0, y_{ij}, 0, \dots, 0]\right)\left(\{a^y\}[\tilde{Y}]\right)^{-1} \quad (9)$$

where $[\tilde{Y}]$ is mode shape of sample model, assembled of SE, y_{ij} is the j-th value of the i-th mode shape.

3. Numerical investigation with application to 1D waveguides

As a numerical example, the analysis of WP in a 1D waveguide is performed. A reference model is assembled of the first order 1D finite elements as

$$[M^e] = \frac{\rho AL}{2}\begin{bmatrix}1 & 0\\ 0 & 1\end{bmatrix} \quad (10.1)$$

$$[K^e] = \frac{EA}{L}\begin{bmatrix}1 & -1\\ -1 & 1\end{bmatrix} \quad (10.2)$$

where A and L – length and respectively cross-sectional area of the element, E is stiffness modulus and ρ is mass density. In 1D case, exact MF and MS of any straight 1D waveguide can be obtained analytically as

$$\omega_{i0} = \pi(i-1)/l\sqrt{E/\rho} \quad (11.1)$$

$$y_{i0j} = \sin\left(\frac{2*pi*(i-1)}{l/(j*L)}\right) \quad (11.2)$$

where i is the mode number, j is number of the component of the i-th MS vector, l is the length of the waveguide. The dimensionless results are obtained by assuming $A = 1$, $E = 1$ and $\rho = 1$. The exact value of the speed of wave is $c = \sqrt{E/\rho} = 1$.

3.1. Obtaining the initial approximation elements

In this numerical experiment IAE, is obtained by substituting (11.1) into (3), while the MS are mapped on the nodes of 10-noded SE. The filling of the mass matrix obtained by (3.1) by non-zero numbers is presented in **Fig. 2a**, and MF errors of the SD assembled of 10 IAE is presented in **Fig. 2b**. The error of each MF is presented as computed by $\frac{\hat{\omega}_i - \omega_{i0}}{\omega_{i0}}$. As the obtained IAE mass matrix is transformed to the diagonal form, the corresponding correction of the stiffness matrix is performed as

$$[\mathrm{K}] = [\mathrm{M}][\mathrm{Y}][\mathrm{diag}(\omega_1, \omega_2, \ldots, \omega_n)][\mathrm{Y}]^{\mathrm{T}}[\mathrm{M}]. \quad (12)$$

The diagonalization of the mass matrix does not significantly change the MF of the SD (**Fig. 2c,d**), therefore further in this work we always use the diagonal form. However, the obtained IAE introduces much bigger MF errors than could be acceptable.

3.2. Minimization of modal frequency errors

The stiffness matrix of SE is obtained by minimizing target function (4) as described in Section 2. After minimization of the target function, the MF errors of the SD are presented in **Fig. 3**. The presented results correspond to different numbers $\tilde{N}$ of MF, the cumulative error of which has been minimized: a) $\tilde{N} = 91$ (100%), b) $\tilde{N} = 63$ (~70%), c) $\tilde{N} = 54$ (~60%), d) $\tilde{N} = 45$ (~50%). Further in this paper the obtained SE are referred to as SE100, SE70, SE60, SE50.

The obtained results in **Fig. 3** should be compared against the MF error curve in **Fig. 2d**. The distribution of MF errors among the modes severely depends on the number of modes the cumulative error of which has been taken into account. In case the cumulative error minimization is performed over all MFs, $\tilde{N} = N$, the result is rather poor, **Fig. 3a**. However, by selecting smaller values of $\tilde{N}$, we may achieve very small values of the cumulative error in this modal range. Probably the best result was obtained as $\tilde{N}$

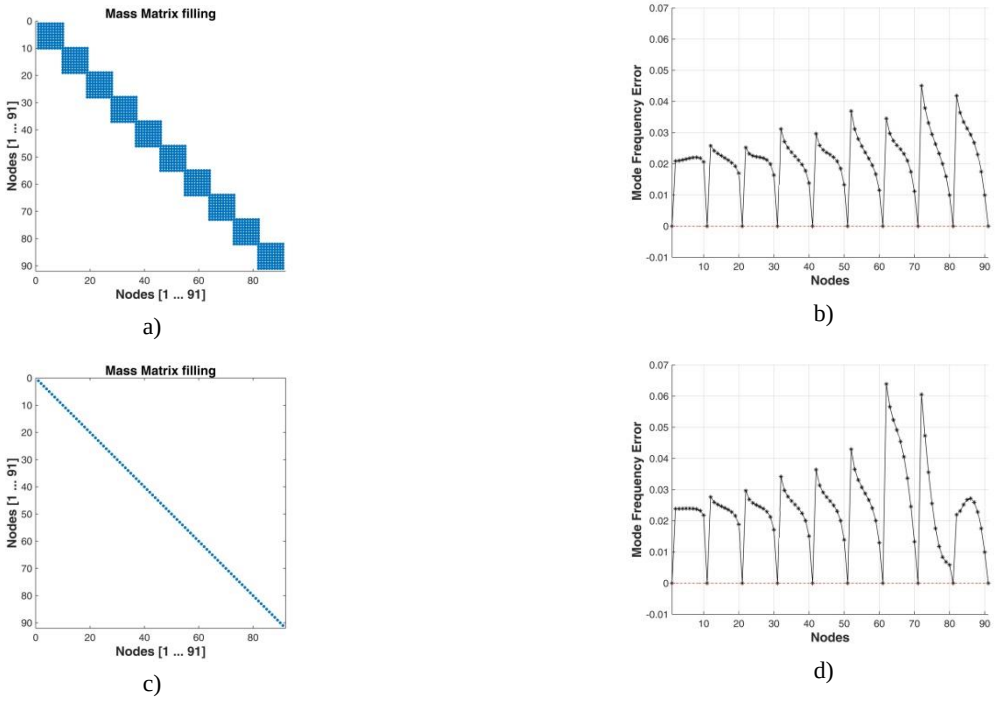

Figure 2. a) Mass matrix filling of the model assembled of 10 IAE 10 nodes each; b) MF errors of the model of 10 IAE; c) The filling of the diagonal mass matrix; d) MF errors of the model with diagonal mass matrix

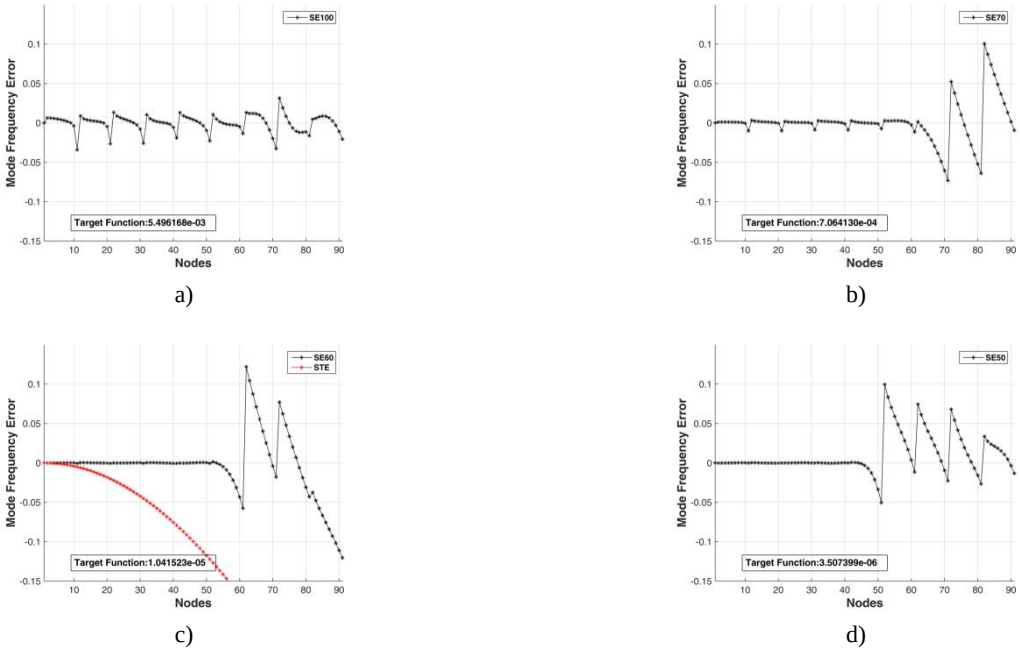

Figure 3. Modal frequency errors of the sample domain assembled of 10 synthesized elements at different numbers of modal frequencies contributing to the cumulative error: a) 100 % (SE100); b) 70% (SE70); c) 60% (SE60); d) 50% (SE50)

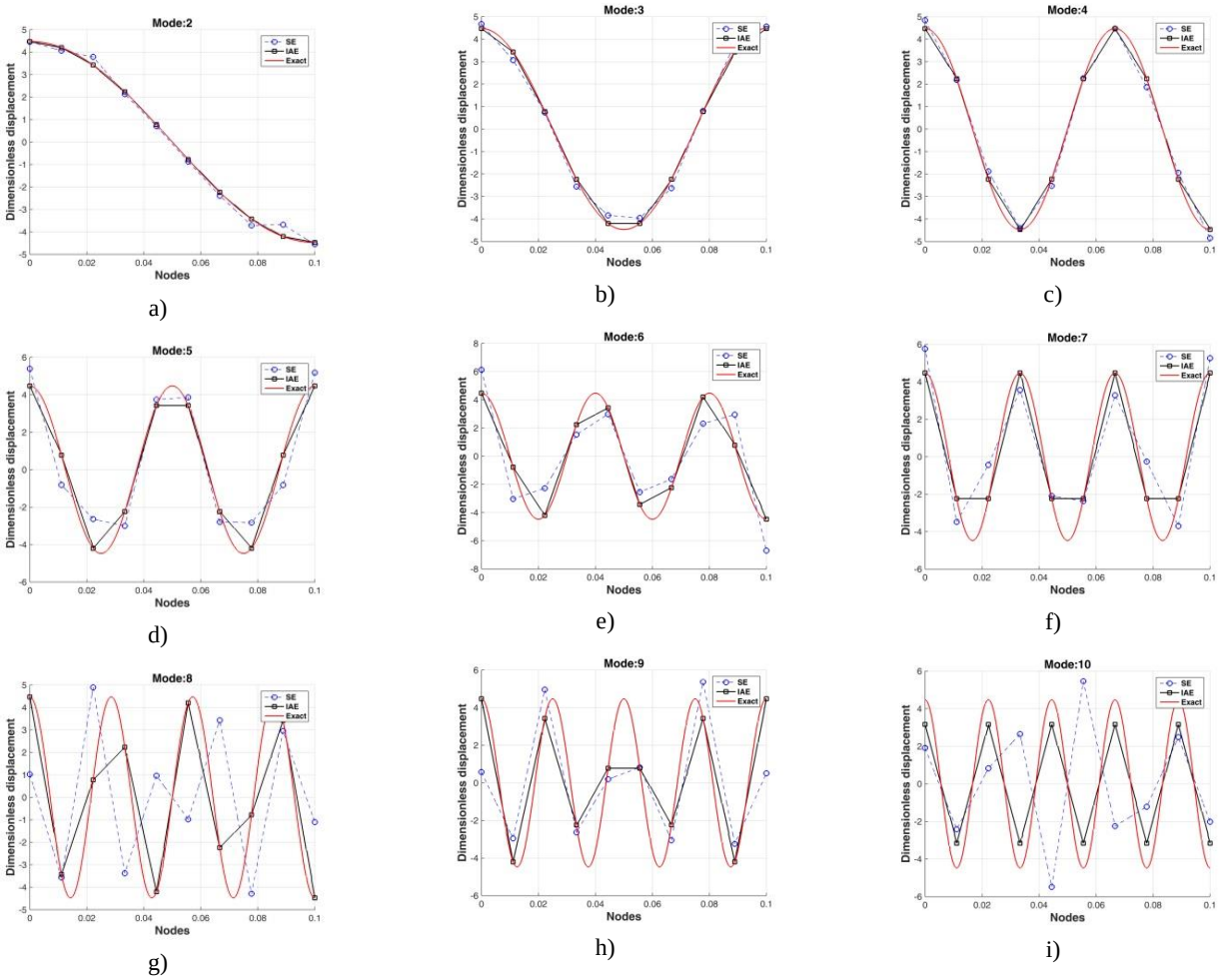

Figure 4. Modified modal shapes of several modes participating in the synthesis of SE60: exact(red smooth line), obtained by direct mapping on the SE (black broken line) , modified by optimization for the synthesis of SE60 (dashed line)

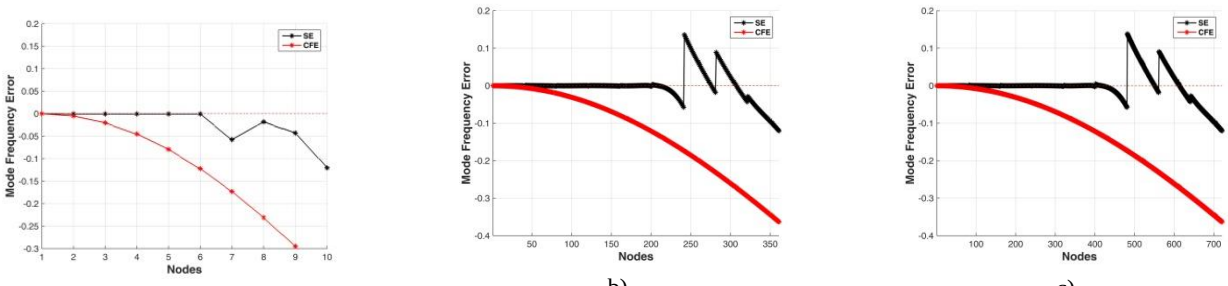

a) b) c)

Figure 5. Errors of MF of models assembled of SE (red) and CFE (black), at different numbers of nodes in the waveguide model: a) N=10; b) N=361; c) N=721

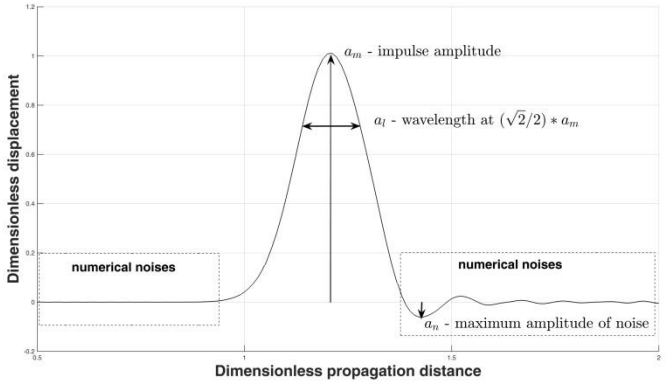

Figure 6. Graphical interpretation of simulation quality indicators $\boldsymbol{a_n}$, $\boldsymbol{a_l}$ and $\boldsymbol{a_m}$

comprised 60% of lower MF, where the final target function value read as $\sum_{i=1}^{\bar{N}} \left(\frac{\bar{\omega}_i - \omega_{i0}}{\omega_{i0}}\right)^2 \approx 10^{-5}$. The modal errors of the higher 40% modes are quite significant, however, further we demonstrate that the overall performance of the model in WP simulations is much better compared against the model of IAEs, and essentially better than could be achieved by using the CFE at the same number of d.o.f., see the red curve of the MF errors in **Fig. 3d**.

It is important to understand what particular modifications defined by coefficients $[a^y]$ undergo the MS mapped on the nodes of the SE in order to achieve the enhanced convergence properties. The modified modal shapes are presented in **Fig. 4**, where modification of the first MS was small, while some higher order MS underwent significant modifications in order to achieve the best cumulative performance.

The values of the obtained modal shape correction coefficients, as well as the mass and stiffness matrices of 1D 10-node SE are presented in Appendices 1 and 2.

A very important property of the investigated models is that the percentage of close-to-exact modes SE does not depend on the overall d.o.f. number of the investigated domain. Approximately, the frequency value of the higher limit of the range of close-to-exact MFs is the same for the stand-alone SE, as well as for the large computational domain assembled of such SE. Therefore the highest close-to-exact modal frequency value of the SE defines the width of wave spectrum, which could be simulated with very small phase velocity errors in waveguide models. **Fig. 5** presents the MF errors of the models of different sizes assembled by using different numbers of nodes as a) $N = 10$; b) $N = 361$; c) $N = 721$. This means that the obtained SE can be used for waveguide structures of different sizes and can be treated as dynamic fast convergent super-element with diagonal mass matrix.

3.3. Simulation of wave pulse propagation

Let us consider the wave pulse is excited at the left-hand end of the 1D waveguide structure and propagates along it. Theoretically, the pulse should move along the structure at the speed of sound, without changing its form. In order to evaluate the extent of deterioration of the pulse shape due to ND errors the following simulation quality indicators are used: wave amplitude a_m at the peak of wave; maximum value of numerical noise (NN) a_n and the width a_l of the pulse at its height $\frac{\sqrt{2}}{2} * a_m$ (**Fig. 6**). In the case of the exact solution we have $a_n = 0$, $a_m = 1$.

Assume the straight 1D structure is assembled of 20 SE, where length of each element $l_e = 0.1$, the total length of the structure $l = 2$, the total number of nodes $N = 181$, the distance between adjacent nodes $L = \frac{l_e}{10-1} \approx 0{,}011$. The dimensionless wave speed is $c = 1$. Simulation is performed during time

period $T = 7\ (s)$, while the distance traveled by the pulse is $S = 7$. The obtained results are compared against the results obtained in the CFE model of the same dimensionality and against the results obtained in a very dense (90 nodes per wavelength) CFE mesh. The latter has been regarded as the close-to-exact solution. The wave simulation is performed by actuating the displacement at the left-hand end of the waveguide as

$$u(t) = \begin{cases} (1 - \cos(\frac{\pi}{deltaT} t)) * deltaU, t < deltaT \\ 0, t \geq deltaT \end{cases} \quad (13)$$

where $deltaT$ is the actuation time, $deltaU$ is the wave amplitude. The dimensionless results are obtained by assuming $deltaU = 1$. The comparison of the results at different space-steps of the model is presented in **Fig. 7**, where propagation distance is expressed in terms of the length of the wave pulse.

It can be observed that in all cases the accuracy of the model assembled of SE is the best with errors less than 10% errors compared against the models of conventional elements. Even 6 nodes per pulse-length in the model assembled of SE produce reasonable simulation results, which are impossible to achieve by using conventional elements at the same mesh density, **Fig. 7d**. The attention should be drawn to the small distortion of the pulse shape at the peak of the pulse as SE with dense mesh (36 nodes per wavelength) were used, **Fig. 7a**. Apparently, it is a consequence of the lower MS correction, which is performed as the element is synthesized. This imperfection exhibits itself at the moment of excitation of the pulse as the mesh is dense. However, the distortion disappears in case a combined model assembled of conventional FE and SE is employed (**Fig. 8**). The explanation is as follows. Both conventional FE and SE meshes ensure the close-to exact MF values, therefore the propagation speed of all harmonic components of the pulse is represented correctly. The representation of the pulse shape depends on MS which are a little distorted in SE. As the pulse comes back to the segment presented by CFE, the distortion of the pulse shape disappears. Practically this distortion is very small, because the corrections of lower MS of the SE are small (**Fig. 4**).

The B-scan image of the wave pulse propagation is presented in **Fig. 9**, where horizontal and vertical axes correspond to the time and to the displacements along

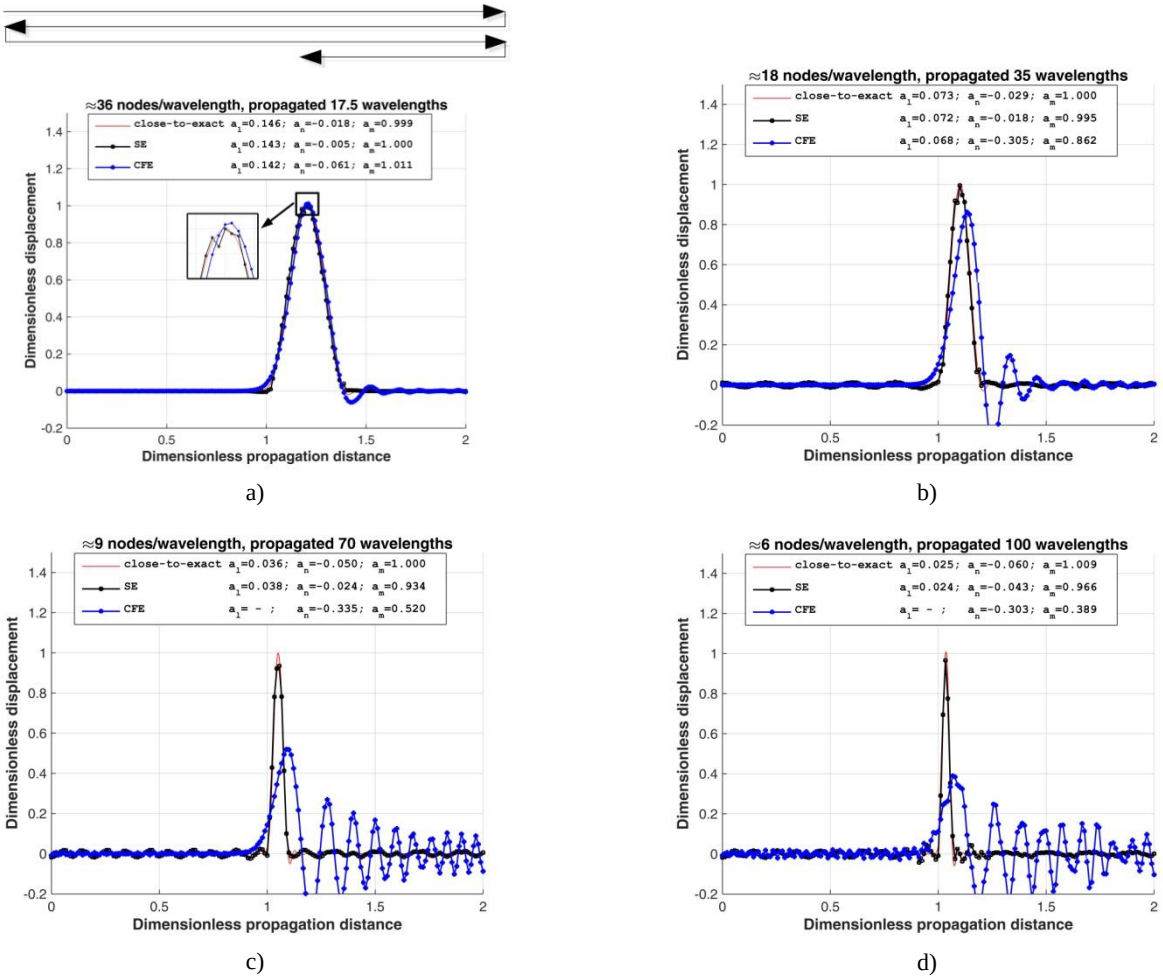

Figure 7. Simulation results after 7 (s): a) $\mathbf{deltaT = 0.4}$, 36 nodes per wavelength, pulse propagated 17.5 wavelengths; b) $\mathbf{deltaT = 0.2}$, 18 nodes per wavelength, pulse propagated 35 wavelengths; c) $\mathbf{deltaT = 0.1}$, 9 nodes per wavelength, pulse propagated 70 wavelengths; d) $\mathbf{deltaT = 0.07}$, ≈6 nodes per wavelength, pulse propagated 100 wavelengths

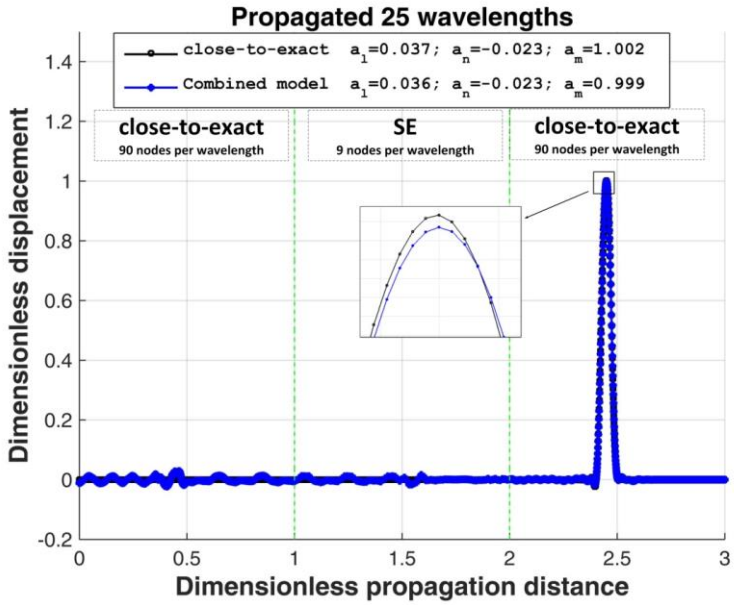

Figure 8. Wave propagation in the combined model assembled of SE60 and STE

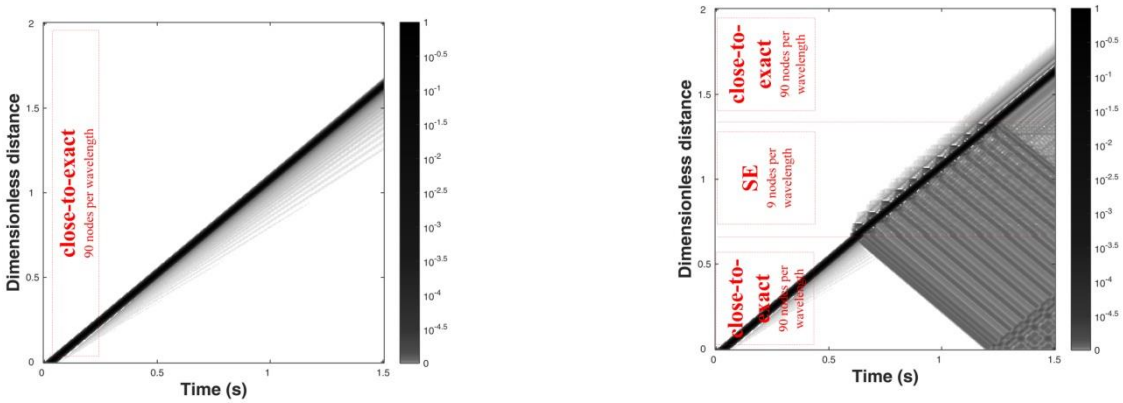

Figure 9. B-scan image with nonlinear color bar of wave simulation in model of a) CFE; b) combined model of CFE and SE60

the waveguide. The intensities of grey-scale represent the magnitude of displacements. In general, NN in the simulation is very small (up to 3% of the amplitude of the pulse), therefore we used the non-linear scale of the color bar. The main difference between the NN generated in both models is that CFE produces errors as a fictitious wave pulses, which are difficult to visually distinguish as the error. Meanwhile in the SE model, the small amplitude NN is distributed over all the structure and its interpretation as the error is much easier.

3.4. Branchy structures containing non-reflecting boundary conditions

In this section, the wave-pulse propagation in branchy non-homogenous model assembled of SE will be investigated. A sample model contains 3 waveguide segments of different properties. The diameters of circular cross-sections are $D_1 = 0.1$, $D_2 = 0.08$ and $D_3 = 0.05$, mass densities $\rho_1 = 0.8$, $\rho_2 = 1.2$, $\rho_3 = 1$, bulk moduli and lengths are $K_{1,2,3} = 1$ and $L_{1,2,3} = 1$. Depending on mass densities, the speeds of the wave are $C_1 \approx 1.12$, $C_2 \approx 0.91$, $C_3 = 1$. The geometry of the investigated domain is presented in **Fig. 10a**.

Simulation starts by actuating the wave pulse as (13) at the left-hand end of segment 1, where deltaT $= 0.1\ (s)$, deltaU $= 1$ (**Fig. 10a**, stage 1). After $\sim 1\ (s)$ the wave-pulse reaches the branching, is partially reflected back and partially continues through segments 2 and 3 (**Fig. 10a**, stage 2). After ~2 (s) the pulse is reflected from the end of segment 2 and comes back, while at the end of segment 3 the non-reflecting boundary condition [15] is implemented (**Fig. 10a**, stage 3) as

$$\sqrt{\frac{K}{\rho}}\frac{\delta u}{\delta x} + \frac{\delta u}{\delta t} = 0. \qquad (14)$$

For comparison of the performance, two models were created. The model assembled of SE contained

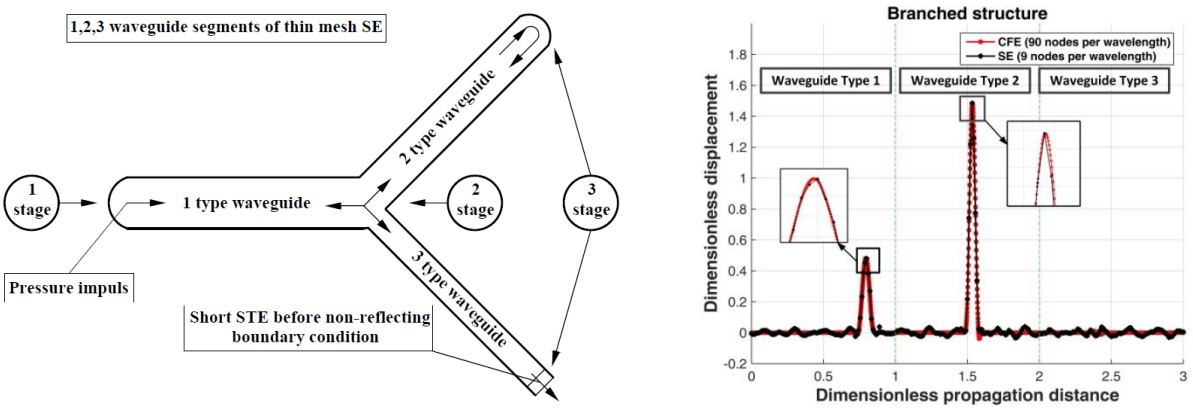

a) b)

Figure 10. a) Geometry of branched non-homogenous structure b) Simulation results after $\mathbf{2.55}$ $(\boldsymbol{s})$

Table 1 Characteristic values of wave-pulse simulation in the branched non-homogenous structure

Waveguide type	Model element type	Nodes per wavelength	a_m	a_n	a_l
TYPE1	SE60	8.3	0.480	0.038	0.042
	STE	82.2	0.481	0.010	0.041
TYPE2	SE60	10.2	1.484	0.039	0.037
	STE	100.6	1.484	0.037	0.034
TYPE3	SE60	9	-	0.038	-
	STE	90	-	0.012	-

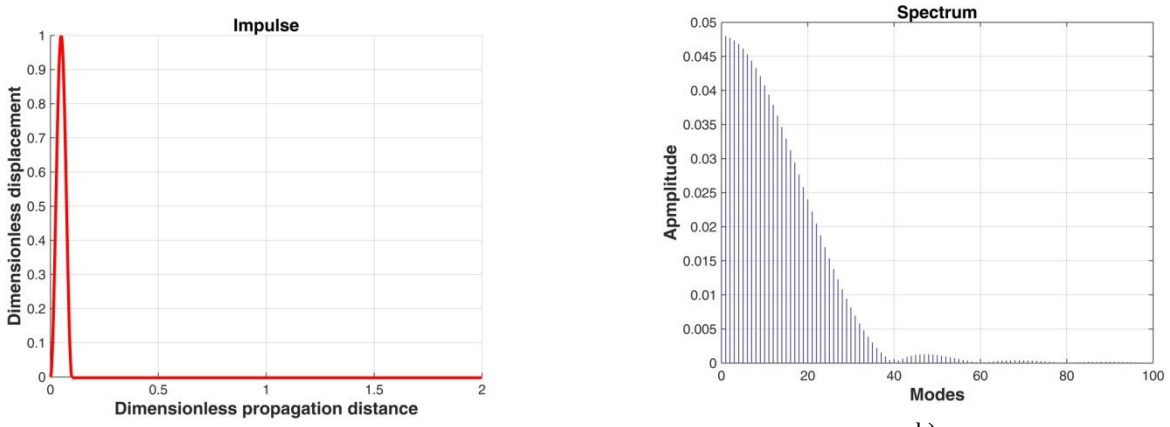

a) b)

Figure 11. a) The shape of the wave pulse; b) Fourier spectrum of the wave pulse

~9 elements per pulse-length, and the model assembled of CFE contained ~90 nodes per pulse-length (close-to-exact solution). The exact number of nodes per pulse-length depends on the mechanical properties of a particular segment (Table 1). As in [12], the non-reflecting boundary condition cannot be implemented in SE directly. Therefore, at the end of segment 3, a short CFE was joined in which the non-reflecting boundary condition can be adequately implemented [10]. Simulation results after 2.55 (s) (at the end of stage 3 in **Fig. 10a**) are presented in **Fig. 10b**. It can be concluded that only negligible discrepancies compared against the reference model could be observed, though the SE60-based model was employed in a quite general and combined situation. The discrepancy between the two models could be estimated as 0.04 relative level numerical noise, which was observed in the SE60-based model. Exact values of the simulation quality indicators a_m, a_n, a_l are presented in **Table 1**.

3.5. Dependencies of results on the frequency spectrum of the propagating wave

We investigate the influence of the number of nodes per pulse length on the accuracy of results of wave simulation, where the models are assembled of

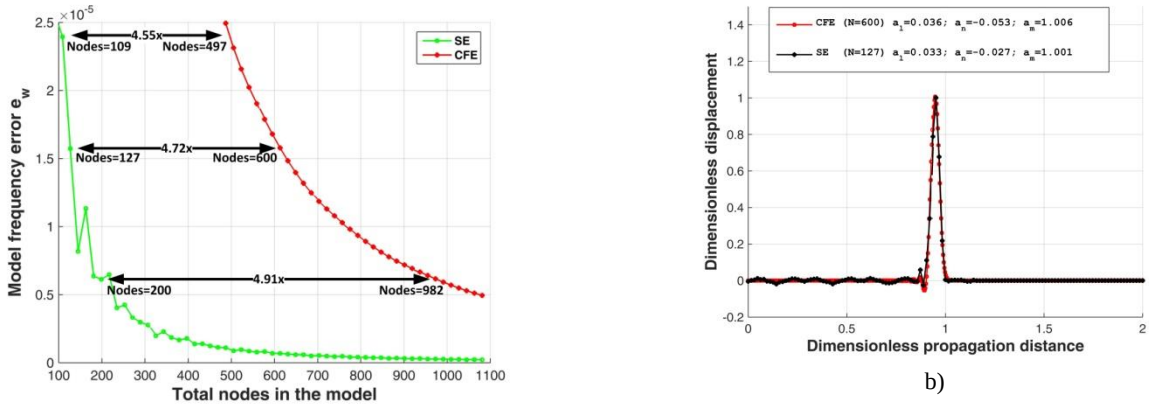

a) b)

Figure 12. Comparison of the e_ω values of the SE60 and CFE models assembled against their number of nodes (a) and Comparison of the shapes of the simulated wave pulse in the SE60 and CFE models at node numbers $N_{SE60} = 127$ and $N_{CFE} = 600$ (equal values of e_ω in both models) (b)

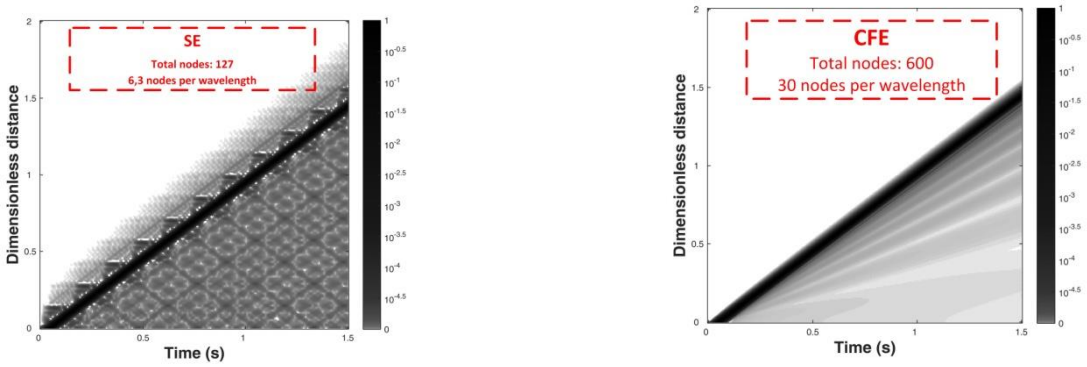

a) b)

Figure 13. Comparison of the B-scan images of the simulated wave pulse in the SE60 and CFE models at node numbers $N_{SE60} = 127$ and $N_{CFE} = 600$ (equal values of e_ω in both models)

SE or of CFE. Assume the wave pulse (13) is actuated in the waveguide of length = 2. In **Fig. 11** the shape and Fourier spectrum of the pulse are presented, where impulse actuation time is $deltaT = 0.1\ (s)$ and the dimensionless wave propagation speed is $C = 1$ (m/s). The width of the Fourier spectrum defines the frequency range, in which the modal frequencies of the model should be close-to-exact in order to provide accurate simulation results. This enables to approximately predict the magnitude of the error of the propagating wave-pulse simulation in terms of modal frequency errors of the finite element structure.

In the case of 1D straight beam, the modal frequencies coincide with the frequencies of the harmonic components of the Fourier spectrum. The error of representation of the propagating wave pulse can be evaluated as

$$e_\omega = \sum_1^N f_i \left(\frac{\hat{\omega}_i - \hat{\omega}_{i0}}{\hat{\omega}_{i0}}\right)^2 \qquad (15)$$

where f_i is the amplitude of the component of the i-th frequency of the Fourier spectrum, $\left(\frac{\hat{\omega}_i - \hat{\omega}_{i0}}{\hat{\omega}_{i0}}\right)^2$ is the relative error of the i-th modal frequency of the structure. The magnitude of e_ω enables to evaluate the amount of the distortion of the shape of the wave pulse. The evaluation is obviously approximate as during the simulation the wave pulse spectrum slightly changes due to the generated NN.

Assume that if e_ω is equal for two different models, their abilities to represent correctly the shape of the propagating wave pulse are the same. In **Fig. 12a** errors e_ω of models assembled of SE and of CFE are compared, while the number of nodes in model varies: $100 \le N \le 1100$.

Fig. 12a demonstrates that e_ω value of the CFE model is the same as e_ω value of the SE model with more than 4.5 times rougher mesh. The performance of the SE model in wave pulse simulation is demonstrated in **Fig. 12b**, where very similar results were obtained by using the CFE model containing $N_{CFE} = 600$ nodes and by using ~4.7 times rougher SE model containing only $N_{SE60} = 127$ nodes. The obtained values of simulation quality indicators a_l, a_n and a_m differ less than 1% between the two models. The same comparison in terms of the B-scan images is presented in **Fig. 13**.

3.6. Comparison of computational resources

In order to obtain the matrices of SE, the minimization problem of target function (4) should be solved. Though the solution of the problem is computationally expensive, the obtained SE60 matrix can be used in any 1D structure as a general result (Appendix 2).

The actual evaluation of the computational resource used for wave simulations includes the amount of memory and the number of operations, which should be performed during each numerical integration step by employing the central difference numerical integration scheme. The SE60 matrices are assumed to be known in advance. The structural matrices assembled of SE and CFE always are sparse matrices. However, the number of non-zero positions in the matrices of the SE model is bigger, as the bandwidth of SE model matrices is equal to the number of nodes of a single SE, while the bandwidth of matrices assembled of CFE is always 3. Depending on required accuracy and the frequency spectrum of the simulated signal, the numbers of nodes in both models of SE and of CFE are different. Assume the propagation of the signal described in section 3.3 is simulated. The number of nodes of the SE model is ~4.7 times less than of the CFE model. Therefore relations between the numbers of nodes and the bandwidths of the stiffness matrices in the two models of the same accuracy read as

$$N_{CFE} = 4.7 * N_{SE} \tag{16.1}$$

$$W_{CFE} = \frac{W_{SE}}{5} = 2 \tag{16.2}$$

where W is the bandwidth of the stiffness matrix.

During the time integration the structural vectors $\{\ddot{U}\}$, $\{\dot{U}\}$, $\{U\}$ and matrices [M], [K] require the memory size as

$$O_{mem} = \left(4N + \frac{N*W+2*N-W}{2}\right) * b \tag{17}$$

where for storage of each number b bytes are allocated. In (17) the diagonal form of [M] and the symmetry of [K] are taken into account.

By combining (16) and (17) we may compare the required computer memory in SE and CFE models as $O_{mem\_CFE} \approx 2.83 * O_{mem\_SE}$, i.e. in SE models the employed memory size is ~65 % less than in CFE models.

The evaluation of the number of operations necessary for the time integration in one integration step by using the central difference scheme is evaluated as

$$O_{st} = 5N * W - 3W. \tag{19}$$

By inserting values (17) into (19) we obtain $O_{st\_CFE} \approx 1.44 * O_{st\_SE}$. This means that SE models require ~30% less arithmetic operations. Practically, computational time depends on machine architecture, operating system, arithmetic operation type, etc. In order to investigate usage of computational resources, numerical experiment of ultrasonic longitudinal wave propagation [13] in 1D aluminum waveguide is performed, where computational times are compared for models assembled of CE and SE60 with 4.7 rougher mesh (30 nodes per wavelength in model of CE and 6.36 in model of SE, respectively). Simulation is performed while pulse propagates whole waveguide, so total time of simulation increases by increasing length of the waveguide. Experiment is performed using Matlab R2015a with sparse mass and stiffness matrices on machine with Intel Core i7-4790 CPU @ 3.60 Hz processor, 32GB RAM and 64-bit Windows Operating System. Physical constants of waveguide of FE model of equation (10) are $E = 71.788$ MPa, $\rho = 2780$ kg/m^3, wave speed 5081 m/s, pulse actuation time 40 μs and integration step 0.4 μs. Results on how the total number of simulation steps and computational time depend on waveguide length are adduced in **Table 2**.

Results in Table 2 show that betterment of computational time obtained by performing simulation is better compared with results obtained by calculating arithmetical operations. Additional advantage of the SE models is bigger value of the limit time step ensuring the stability of the numerical integration scheme.

4. Conclusion

The main result of this work is that the method based on modal synthesis allowed to develop the dynamic super-elements, the convergence properties of which are much better if compared against conventional finite elements. Better convergence properties allow much rougher meshes for simulations of short waves propagation in large structures while retaining similar accuracy. Another point is that the of short

Table 2. Comparison of computational times using FE models assembled of CE and SE60

Waveguide length (m)	Simulation time (ms)	Total simulation steps	Model of CE		Model of SE60		Betterment (%)
			Nodes	Computational time (s)	Nodes	Computational time (s)	
10	1.97	4920	1476	0.158	316	0.083	47
20	3.94	9839	2952	0.551	622	0.305	45
50	9.84	24598	7380	3.366	1567	1.571	53
100	19.68	49197	14759	13.607	3124	6.907	49
200	39.58	98394	29518	56.966	6256	23.982	58

waves propagation in large structures while retaining similar accuracy. Another point is that the numerical errors generated by new elements tend to be distributed equally over the domain behind the travelling wave pulse. On the contrary, the numerical errors generated by conventional elements often resemble one or several wave pulses of considerable amplitude, which follow the main wave and sometimes can be misinterpreted by regarding them as real rather than fictitious. Though the principle was demonstrated already in our previous researches, the mass matrices of synthesized elements obtained in this work are diagonal and therefore may be fully functional in explicit time integration schemes. The synthesized elements can be treated as higher-order finite elements, though the synthesis procedure did not require explicit determination of higher order shape functions. It is important that the synthesized elements may be used in combination with conventional elements and in branchy non-homogenous structures, as well as enable to implement non-reflecting boundary conditions, which are important in many engineering applications. Here we demonstrated the full functionality of the created elements in 1D case, however, the synthesis procedure is essentially the same in 2D and 3D cases. This research is under way now.

Acknowledgment

The research has been sponsored by the Lithuanian Science Council, Agreement Number MIP-044/2014.

References

[1] **R. Barauskas, R. Barauskiene.** Highly Convergent Dynamic Models Obtained by Modal Synthesis with Application to Short Wave Pulse Propagation. *International Journal for Numerical Methods in Engineering*, 2004, Vol.61, No.14, 2536–2554.

[2] **R. Barauskas**. On Highly Convergent 2D Acoustic and Elastic Wave Propagation Models. *Communications in Numerical Methods in Engineering*, 2005, Vol.22, No.3, 225–233.

[3] **I. Bartoli, A. Marzani, F. L. Scalea, E. Viola.** Modeling Wave Propagation in Damped Waveguides of Arbitrary Cross-Section. *Journal of Sound and Vibration*, 2006, Vol.295, No.3, 685-707.

[4] **X. Chen, Z. Yang, X. Zhang, Z. He.** Modeling of wave propagation in one-dimension structures using B-spline wavelet on interval finite element. *Finite Elements in Analysis and Design* 2012, Vol.51, 1-9.

[5] **H. Seounghyun, K. Bathe.** A finite element method enriched for wave propagation problems. *Computers & Structures*, 2012, Vol.94, 1-12.

[6] **R. Hill, S. A. Forsyth, P. Macey.** Finite element modelling of ultrasound, with reference to transducers and AE waves. *Ultrasonics*, 2004, Vol.42, No.1, 253-258.

[7] **R. Khajavi.** General templates for n-noded bar elements based on reduced representations and numerical dispersion reduction by optimized finite elements. *Applied Mathematics and Computation*, 2014, Vol.233, 445-462.

[8] **H. Kohno, K. Bathe, J. C. Wright.** A finite element procedure for multiscale wave equations with application to plasma waves. *Computers & Structures*, 2010, Vol.88, No.1, 87-94.

[9] **R. Kolman, J. Plešek, M. Okrouhlík.** Complex wavenumber Fourier analysis of the B-spline based finite element method. *Wave Motion*, 2014, Vol.51, No.2, 348-359.

[10] **A. Krisciunas, R. Barauskas.** Minimization of Numerical Dispersion Errors in Finite Element Models of Non-homogeneous Waveguides. *Information and Software Technologies*, 2013, Vol.403, 357-364.

[11] **A. Monorchio, E. Martini, G. Manara, G. Pelosi.** A dispersion analysis for the finite-element method in time domain with triangular edge elements. *IEEE Antennas and Wireless Propagation Letters*, 2005, Vol.1, No.1, 207-210.

[12] **T. Oha, J. S. Popovicsa, S. Hama, S. W. Shinb.** Practical finite element based simulations of nondestructive evaluation methods for concrete. *Computers & Structures*, 2012, Vol.98, 55-65.

[13] **J. Prikšaitis, L. Mažeika, R. Barauskas, E. Žukauskas, A. Kriščiūnas.** Influence of the Numerical Dispersion Effects in the Modelling of Ultrasonic Measurements. *Physics Procedia*, 2015, Vol. 70, 532-536.

[14] **Y. Shen, S. Hirose, Y. Yamaguchi.** Dispersion of ultrasonic surface waves in a steel–epoxy–concrete bonding layered medium based on analytical, experimental, and numerical study. *Case Studies in Nondestructive Testing and Evaluation*, 2014, Vol.2, 49-63.

[15] **J. P. Wolf, C. Song.** Finite-element modelling of unbounded media. Chichester Wiley, 1996.

[16] **W. Tingting, Z. Chen.** A dispersion minimizing subgridding finite difference scheme for the Helmholtz equation with PML. *Journal of Computational and Applied Mathematics*, 2014, Vol.267, 82-95.

[17] **B. Xu, Z. Shen, X. Ni, J. Lu.** Numerical simulation of laser-generated ultrasound by the finite element method. *Journal of Applied Physics, 2004*, Vol.95, 2116-2122.

[18] **A. Żak, M. Krawczuk.** Certain numerical issues of wave propagation modelling in rods by the Spectral Finite Element Method. *Finite Elements in Analysis and Design*, 2011, Vol.47, No.9, 1036-1046.

Received November 2015.

Appendix 1. Examples of mode shape correction coefficients.

$[a_y] =$

1.0000	0.9990	1.0091	1.0165	1.4052	1.3402	1.0269	1.1935	1.2459	1.3579
1.0000	0.9799	0.9096	0.9097	0.9268	1.1102	1.1612	1.1948	1.1681	1.4522
1.0000	1.1247	1.0932	0.9004	0.5874	0.6974	0.8417	0.9824	0.9906	1.1330
1.0000	0.9766	1.1159	0.9899	1.2080	1.0209	1.0090	0.9790	1.0135	1.0048
1.0000	0.9700	0.9803	1.0749	1.0162	0.8932	0.9992	1.0393	0.9422	0.9953
1.0000	0.9842	0.9997	1.0887	1.0210	0.8816	1.0193	1.0455	0.9301	0.9953
1.0000	1.0228	1.1463	1.0364	1.2041	1.0253	1.0012	0.9412	1.0361	1.0043
1.0000	1.0725	1.0201	0.8701	0.6416	0.6948	0.8201	0.9623	0.9888	1.1189
1.0000	0.8731	1.0255	0.8999	0.9321	1.1111	1.2293	1.1745	1.1634	1.4718
1.0000	1.0064	0.9260	1.0495	1.3628	1.3492	1.1042	1.1493	1.1924	1.3689

Appendix 2. 10-node SE60 mass and stiffness matrices

$[M_{SE60}] = \frac{\rho AL}{2} *$

0.0556	0	0	0	0	0	0	0	0	0
0	0.1111	0	0	0	0	0	0	0	0
0	0	0.1111	0	0	0	0	0	0	0
0	0	0	0.1111	0	0	0	0	0	0
0	0	0	0	0.1111	0	0	0	0	0
0	0	0	0	0	0.1111	0	0	0	0
0	0	0	0	0	0	0.1111	0	0	0
0	0	0	0	0	0	0	0.1111	0	0
0	0	0	0	0	0	0	0	0.1111	0
0	0	0	0	0	0	0	0	0	0.0556

$[K_{SE60}] = \frac{EA}{L} *$

9.3797	-9.5509	-1.2418	2.8376	-2.3629	0.9749	0.2604	-0.1870	-0.0050	-0.1051
-9.5509	26.8624	-19.0860	0.4962	6.0841	-4.9360	1.6100	-1.2386	-1.4587	1.2175
-1.2418	-19.0860	35.4778	-16.3809	-3.2694	3.1376	-1.7022	5.5551	-2.2209	-0.2693
2.8376	0.4962	-16.3809	26.8183	-15.3426	4.0553	-1.9451	-2.9635	2.4652	-0.0404
-2.3629	6.0841	-3.2694	-15.3426	32.0945	-20.7370	3.9507	2.9985	-4.2881	0.8720
0.9749	-4.9360	3.1376	4.0553	-20.7370	32.1867	-15.3382	-2.8368	6.1346	-2.6412
0.2604	1.6100	-1.7022	-1.9451	3.9507	-15.3382	26.4182	-17.1129	1.5830	2.2762
-0.1870	-1.2386	5.5551	-2.9635	2.9985	-2.8368	-17.1129	36.1063	-19.2508	-1.0703
-0.0050	-1.4587	-2.2209	2.4652	-4.2881	6.1346	1.5830	-19.2508	26.6511	-9.6102
-0.1051	1.2175	-0.2693	-0.0404	0.8720	-2.6412	2.2762	-1.0703	-9.6102	9.3708